

An Integrated MEMS Magnetic Gradiometer Rejecting Vibrations and Stray Fields

Enrico Gasparin¹, Arno Hoogerwerf², Dara Bayat², Guido Spinola Durante²,
Yves Petremand², Maurizio Tormen¹, Michel Despont² and Gaël Close^{1,*}

¹Melexis Technologies SA, Bevaix, Switzerland

²CSEM SA, Neuchâtel, Switzerland

*Corresponding author: gcl@melexis.com

Abstract—Due to electrification, magnetic sensors are increasingly deployed in magnetically polluted environments. To reject stray fields, differential sensing schemes are typically used. In this paper, we rely instead on a single-point gradiometric sensing scheme based on the force exerted on a magnet, which is directly related to the magnetic field gradient. Unlike the prior art, our concept uses a differential MEMS force-sensing mechanical transducer. The overall sensor rejects not only magnetic stray fields, but also mechanical disturbances such as vibration and gravity. It is the first single-point MEMS gradiometer that can operate unshielded in various orientations. Our prototype realization achieves a noise density of 4 nT/mm/√Hz in a ±300 μT/mm measurement range. We demonstrate its operational effectiveness in a bus-bar current sensing application. Finally, the paper discusses the remaining weaknesses and provides an outlook for MEMS-based magnetic sensors.

Index Terms—Micromechanical devices, magnetic sensors.

I. INTRODUCTION

A. Context

In our increasingly electrified world, high-power currents and electrical motors abound. They generate magnetic stray fields, which could interfere with the 10-billion magnetic sensors produced annually [1]. Such sensors are ubiquitous in automotive, industrial, and residential applications to measure the position of a magnet or electric current [2]. For proper operation, despite the increasing magnetic disturbances, there is a need to develop stray-field-immune magnetic sensors. The parasitic magnetic stray fields are typically rejected via differential operation by combining several sensing locations [3]. This approach results in magnetic gradiometers: sensors measuring some components of the magnetic field gradient, for example, $\partial B_x / \partial x$. Recently, another approach emerged based on a magnet mounted on a MEMS force-sensing transducer [4]. In this arrangement, the force exerted on the magnet (with a magnetic moment \mathbf{M}) is directly proportional to the magnetic field gradient $\mathbf{F} = \nabla(\mathbf{B} \cdot \mathbf{M})$, while the uniform stray fields generate a torque $\boldsymbol{\tau} = \mathbf{B} \times \mathbf{M}$. In layman's terms, a magnet moves as opposite poles attract and rotates to align itself with the field lines. The undesirable torque can be mitigated by enhancing the rigidity of the MEMS structure against rotational forces. Hence, the rejection of uniform stray fields is accomplished directly in the transducer and not via an explicit

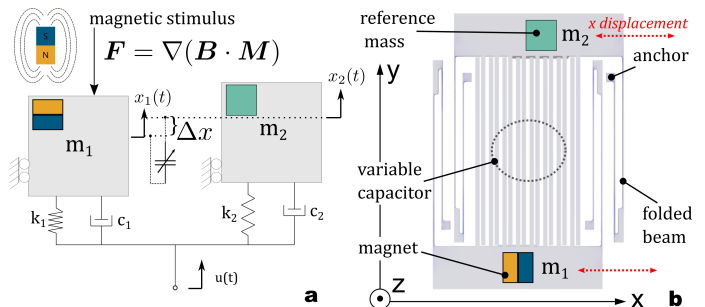


Fig. 1: (a) Free body force diagram. (b) Sensor schematic.

subtraction operation in the signal chain. This enables a single-point magnetic gradiometer with a built-in rejection of uniform stray fields. This approach introduces new challenges due to the mechanical nature of the device. Gravity and vibrations directly leak into the signal chain without attenuation. There is a need to study mechanically robust MEMS gradiometers that reject these disturbances.

B. Sensor requirements

The purpose of this work is to develop a robust single-point MEMS gradiometric sensor resolving $< 10 \text{ nT/mm}/\sqrt{\text{Hz}}$ of field gradient and measuring up to a full scale $\text{FS} = 300 \mu\text{T/mm}$. For instance, this would provide more than 8 bits of noise-free resolution (NFR) in a 500-Hz bandwidth. This field gradient resolution would be competitive with two fluxgates assembled on either side of a PCB in [5] (intended to be inserted in a hole in a bus bar to sense current). It would also outperform the Giant Magneto Impedance (GMI) gradiometer in [6], while providing two orders of magnitude improvement with respect to commercial Silicon Hall and Tunneling Magneto Resistance (TMR) integrated gradiometers in [7], [8] respectively. The sensor should operate in any orientation without mechanical or magnetic shielding, even in the presence of typical environmental vibrations and stray magnetic fields.

C. Preview

This paper extends the pioneering work in [4] by introducing, in Section II, a differential mechanical transducer, illustrated in Fig. 1(a). The compliant MEMS structure includes a

non-magnetic reference mass matching the magnet mass. Section III describes the sensor implementation and the magnet assembly process. The experiments in Section IV show that the mechanical disturbances appear as common-mode forces and are rejected. The resulting single-point MEMS gradiometer is compared against other gradiometers in Section V, and is the first of his class that can operate unshielded in various orientations. The paper concludes by providing the design outlook for this class of MEMS gradiometers.

II. SENSOR DESIGN

Similar to the pioneering work in [4], the sensor is based on the transduction of the magnetic force acting on a cubic NdFeB magnet of side length $250\ \mu\text{m}$, with mass $m = 125\ \mu\text{g}$ and magnetic moment $M_z = 15\ \mu\text{J}/\text{T}$. To obtain an intuitive sense of the extent of this force, we can compare it to gravity. The gravity exerts on the magnet a force equal to $1.23\ \mu\text{N}$. A full-scale gradient $\text{FS} = 300\ \mu\text{T}/\text{mm}$ produces $4.5\ \mu\text{N}$, only about 3.5 times greater than the gravitational force. In other words, the relative gravity error is approximately 30%FS, when expressed relatively to the full-scale upper limit. To obtain a robust sensor in the targeted range, the effects of gravity and other parasitic accelerations of similar magnitude must be rejected further. A single-ended device like [4], being intrinsically sensitive to both gravity and magnetic forces, is bound to be fragile and restricted to the lab.

By contrast, our proposed concept exploits the mass balance principle for additional rejection, as depicted in Fig. 1. Two uncoupled structures form the electrodes of a variable capacitor. They are supported by folded beams as compliant elements. Only linear displacements are allowed. The structures are rigid against twists. One is tied to the magnet, while the other is tied to an equivalent non-magnetic mass. The two structures are mechanically equivalent (same mass, same springs) and uncoupled. The magnetic force displaces only the magnet and its corresponding electrode. The net differential displacement is transduced into a capacitance change. On the other hand, mechanical accelerations induce common-mode displacements with no impact on the capacitance. Hence, mechanical accelerations are largely rejected, up to a degree limited by the matching between the two masses. Rotational accelerations and torques due to uniform stray magnetic fields are also rejected thanks to the rigidity against twists. Overall, the capacitive response is largely determined by the magnetic field gradient, while mechanical accelerations and stray fields are second-order effects (around 1%FS).

The structures are patterned as array of interdigitated combs with μm -size gaps to maximize the capacitive response. High-fidelity simulations in Comsol Multiphysics were conducted to optimize the linearity of the displacement and the rejection of disturbances. The thickness-to-width ratio of the beams supporting the magnet and the matching mass should be at least 10:1 to keep the out-of-plane movements two orders of magnitude smaller than the in-plane movements. Electrical simulations were used to calculate the capacitance of the

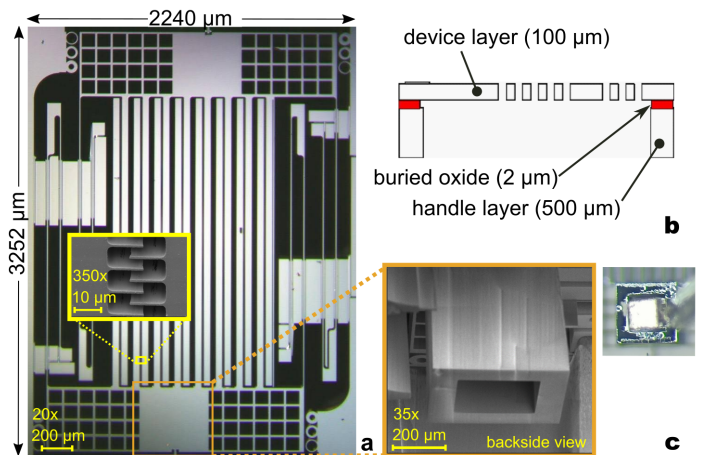


Fig. 2: (a) SEM image of the front side of the implemented device. The inset shows the interdigitated combs. (b) Layers definitions. (c) Backside cavity used as magnet holder.

interdigitated combs and its sensitivity to differential displacements. Combining the magnetic, mechanical, and electrical simulations, the gradiometer sensitivity was simulated to be $6.4\ \text{aF}/(\text{nT}/\text{mm})$.

III. IMPLEMENTATION

The MEMS magnetometer was manufactured on an SOI wafer, with a device layer thickness of $100\ \mu\text{m}$, a buried oxide layer of $2\ \mu\text{m}$, and a handle layer of $500\ \mu\text{m}$. The fabrication process, with a minimum feature size of $2\ \mu\text{m}$, involves two front-side Deep Reactive Ion Etching (DRIE) steps to independently optimize spring constants and capacitor surfaces, along with one backside DRIE step to create a cubic opening for the micromagnet allocation. The device design incorporates interdigitated structures to minimize area consumption, folded springs for the movable membranes to ensure pure translation without rotation, and horizontal and vertical shock stoppers. Furthermore, the geometry of the silicon membrane not bearing the micromagnet was adjusted to optimize the mass equalization with the silicon membrane carrying the micromagnet. Fig. 2 shows SEM images of the front side of the device, together with the detailed dimensions of interdigitated fingers and the cavity used as a magnet holder. After wafer dicing, a NdFeB cubic magnet of $250\ \mu\text{m}$ side length was inserted into the backside cavity and glued in place with epoxy. The dies were wire-bonded in a non-magnetic LCC44 package above a 3D-printed plastic stand-off allowing the free movement of the mass and the magnet. A glass lid was used as dust protection. The readout of the capacitance was done off-chip using an off-the-shelf AD7745 capacitance-to-digital converter.

IV. EXPERIMENTAL RESULTS

A. Response to magnetic field gradients

An arrangement of custom-designed biplanar Maxwell coils [9], with a gradient magnetic constant $k_g =$

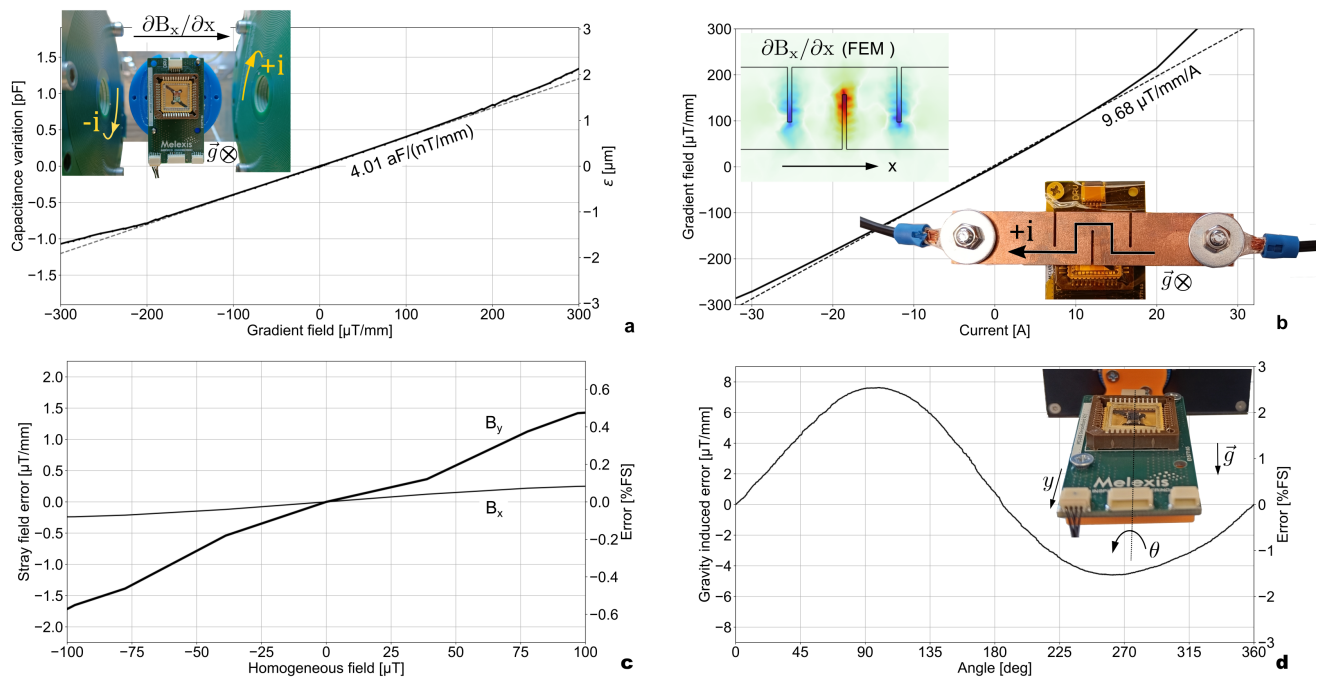


Fig. 3: (a) Response to field gradients. (b) Current sensing demonstration. (c) Stray-field error for different field orientations. (d) Residual gravity error for a full device rotation.

$0.25 \mu\text{T}/(\text{mm} \cdot \text{mA})$, was used to characterize the device sensitivity and linearity in the defined range ($\pm 300 \mu\text{T}/\text{mm}$). The capacitive response curve ΔC vs. $\partial B_x / \partial x$ and a picture of the setup are shown in Fig. 3a. A linear fitting of the curve provided the capacitive sensitivity of the gradiometer: $4.01 \text{ aF}/(\text{nT}/\text{mm})$, about 63% of the design expectation. We attribute this discrepancy to improper process control of the etching steps. The linearity error exhibited an exponential trend and remained below $\pm 5\%$ FS. We speculate that the overlap of interdigitated combs is larger than anticipated, increasing the spurious contribution of the fringing capacitance. The equivalent magnetic noise density was calculated from the standard deviation of the capacitance response and the sensitivity, yielding an average value of $B_n = 3.87 \text{ nT}/\text{mm}/\sqrt{\text{Hz}}$.

B. Current sensing demonstration

To demonstrate the device's operational capability as a gradiometric current sensor, it was placed underneath a bus bar with a snake-shaped slot. The slot forces the current to flow in a S-shaped trajectory, resulting in a strong localized field gradient ($8.9 \mu\text{T}/\text{mm}/\text{A}$ at 2.2 mm above the bus bar, as per Comsol simulation). The response curve ($\partial B_x / \partial x$ readout from sensor versus the current in the bus bar) and the setup are shown in Fig. 3b. The extracted gradiometric current sensor sensitivity matches the Comsol simulation. Combining the sensitivity and the noise results, the gradiometric current sensor can resolve $\approx 400 \mu\text{A}/\sqrt{\text{Hz}}$.

C. Response to uniform stray magnetic fields

The device was placed in a setup consisting of a Helmholtz coil pair, capable of generating a uniform stray field B_{stray} .

The stray-field error is shown in Fig. 3c. The case where the uniform field is in the y direction is the least favorable, as expected. In this case, the parasitic torque $\tau = \mathbf{B} \times \mathbf{M}$ is maximum, and twists the MEMS structures. Due to non-idealities, this parasitic motion leaks into the capacitive readout path and is misinterpreted as a gradient (a field difference ΔB over the length d of the magnet). The calculated Common Mode Rejection Ratio was $\text{CMRR} = \Delta B / B_{\text{stray}} \approx 47.4 \text{ dB}$. The case where the uniform field lies in the x direction is more favorable (extra +20 dB of rejection), because the parasitic torque is ideally zero due to geometrical considerations.

D. Influence of gravity

To quantify the impact of gravity, we rotated the device together with the gradient-generating coils and recorded the offset and gradient sensitivity. The gravity causes an inconsequential $1.2 \mu\text{m}$ common-mode displacement of the magnet and the reference mass. Due to mass mismatch, a differential displacement also occurs. Fig. 3 shows the parasitic change of the offset for a full revolution around the y axis. The parasitic change resembles a sinewave with an amplitude of 2.5% FS, indicating a $4.82 \mu\text{g}$ of equivalent mass unbalance, or approximately 4% of the magnet mass.

V. DISCUSSION

A. Benchmark against other integrated gradiometers

To put our results in perspective, the sensor performance parameters are benchmarked against state-of-the-art integrated gradiometers in Table I. We follow the same convention as the survey in [9]. The parameter d is the distance between

the sensing spots (≤ 2 mm for integrated gradiometers). For our single-point gradiometer, we take the magnet length. B_{\max} is the full-scale gradient, while B_n is the equivalent noise gradient in a 500-Hz bandwidth by convention. The competitors are arranged in order of increasing noise. Fig. 4 plots B_{\max} vs B_n , depicting the classic trade-off between range and precision, for a fixed resolution in bits $NFR = \log_2 \frac{2B_{\max}}{6.6B_n}$. Starting from the bottom left, the MEMS gradiometer in [4] offers the best precision at the expense of a limited full-scale. Due to the absence of a mass-compensating structure and hinge mechanics that would enable pure translation, this device lacks robustness against accelerations, vibrations, and stray fields. As a result, it is only operable horizontally and necessitates a 20-dB magnetic shield. In terms of precision, our experimental device is competitive with the dual fluxgate gradiometer (2 sensor chips back-to-back on either side of a PCB) in [5] and GMI sensor in [6]. This is visualized by the relative proximity of the corresponding symbols in the plot. In the top-right corner, far from our precision target, we find the two commercial integrated gradiometers in [7], [8]. These are robust automotive products, offering excellent stray-field rejection thanks to the good matching between the two sets of Hall plates or TMR transducers at either end of the chip. The high-speed TMR current sensor in [8] also shines in bandwidth (1 MHz). Overall, our prototype is competitive magnetically with the fluxgate and GMI sensors, despite the recent emergence of the MEMS gradiometer concept.

B. Limitations and design outlook

Despite largely improving the robustness of MEMS gradiometers, our work did not address the limited bandwidth. In our present prototype, the bandwidth is limited by the mechanical resonance frequency (around 200 Hz). An optimized MEMS design like [10] with a stiffer structure and a smaller gap between the capacitive electrodes could enable a bandwidth approaching 10 kHz. A tighter integration of the capacitive interface IC with the MEMS structure would enable us to recover the 2 or 3 bits of noise-free resolution that we lost due to the long wire bonds. The capacitive noise floor of our implementation was $10 \text{ aF}/\sqrt{\text{Hz}}$, instead of $1 \text{ aF}/\sqrt{\text{Hz}}$ in [10]. Another avenue for improvement would be the integration of wafer-level fabricated micromagnets with lithographically defined dimensions [11]. It would improve the matching with

the reference mass, and hence the rejection of accelerations, and provide room for miniaturization.

VI. CONCLUSION

We demonstrated a proof-of-concept single-point MEMS gradiometer based on a novel differential mechanical structure. Our prototype operates without mechanical or magnetic precautions in an office environment. It can be used, among other applications, as a gradiometric current sensor. Compared to state-of-the-art MEMS gradiometers, our prototype is substantially more robust, reducing parasitic mechanical accelerations and stray fields to second-order effects. It is competitive magnetically with established technologies like fluxgate and GMI. The remaining limitations could be addressed with technology and design co-development, exploiting the recent advances in high-bandwidth MEMS accelerometers and micromagnets. Overall, this paper opens a new avenue for robust MEMS-based integrated gradiometers.

REFERENCES

- [1] P. Delbos and D. Damianos, "Magnetic sensor: Market and technology report 2022," Yole Développement, Tech. Rep., 2022. [Online]. Available: <https://s3.i-micronews.com/uploads/2022/03/YINTR22255-Magnetic-Sensor-2022-Product-Brochure.pdf>
- [2] P. Ripka, "Contactless measurement of electric current using magnetic sensors," *tm - Technisches Messen*, vol. 86, no. 10, pp. 586–598, Oct. 2019, doi:10.1515/teme-2019-0032.
- [3] S. Huber, J.-W. Burssens, N. Dupré, O. Dubrulle, Y. Bidaux, G. Close, and C. Schott, "A gradiometric magnetic sensor system for Stray-Field-Immune rotary position sensing in harsh environment," in *Proceedings of Eurotsensors 2018*, vol. 2, Dec. 2018, p. 809, doi:10.3390/proceedings2130809.
- [4] J. Javor, A. Stange, C. Pollock, N. Fuhr, and D. J. Bishop, "100 pt/cm single-point MEMS magnetic gradiometer from a commercial accelerometer," *Microsystems & Nanoengineering*, vol. 6, no. 1, pp. 1–13, Aug. 2020, doi:10.1038/s41378-020-0173-z.
- [5] S. Vestal, *Design Considerations for Dual DRV425 Bus Bar Application*, Apr. 2017. [Online]. Available: <https://www.ti.com/lit/ab/sboa185/sboa185.pdf>
- [6] Rohm, *BM14270AMUV-LB Current Sensor IC Datasheet*, Rev.001, Oct. 2019. [Online]. Available: https://fscdn.rohm.com/en/products/databook/datasheet/ic/sensor/current_sensor/bm14270amuv-lb-e.pdf
- [7] N. Dupré, Y. Bidaux, O. Dubrulle, and G. Close, "A stray-field-immune magnetic displacement sensor with 1% accuracy," *IEEE Sens. J.*, vol. 20, no. 19, pp. 11 405–11 411, May 2020, doi:10.1109/JSEN.2020.2998289.
- [8] Allegro, "CT452 datasheet: XtremeSense® TMR coreless, differential and contactless current sensor with programmable gain," CT452-DS Rev. 2, 2024. [Online]. Available: <https://www.allegromicro.com/-/media/files/datasheets/ct452-datasheet.pdf>
- [9] B. Brajon, E. Gasparin, and G. Close, "A benchmark of integrated magnetometers and magnetic gradiometers," *IEEE Access*, vol. 11, pp. 115 635–115 643, 2023, doi:10.1109/ACCESS.2023.3325035.
- [10] Y. Jeong, D. E. Serrano, and F. Ayazi, "A wide-bandwidth tri-axial pendulum accelerometer with fully-differential nano-gap electrodes," *Journal of Micromechanics and Microengineering*, vol. 28, no. 11, p. 115007, sep 2018, doi:10.1088/1361-6439/aadc7e.
- [11] M. T. Bodduluri, B. Gojdka, N. Wolff, L. Kienle, T. Lisec, and F. Lofink, "Investigation of Wafer-Level fabricated permanent micromagnets for MEMS," *Micromachines (Basel)*, vol. 13, no. 5, May 2022, doi:10.3390/mi13050742.

TABLE I: Benchmark of key performance parameters.

	This work	[4]	[5]	[6]	[7]	[8]
Techno.	MEMS	MEMS	Fluxgate	GMI	Silicon Hall	TMR
d	250 μm	250 μm	2.00 mm	500 μm	2.00 mm	700 μm
B_{\max}	300 $\mu\text{T}/\text{mm}$	460 nT/mm	2.00 mT/mm	560 $\mu\text{T}/\text{mm}$	12.0 mT/mm	8.57 mT/mm
B_n	86.5 nT/mm	439 pT/mm	23.7 nT/mm	390 nT/mm	2.68 $\mu\text{T}/\text{mm}$	2.91 $\mu\text{T}/\text{mm}$
NFR	10.0 b	8.31 b	14.6 b	8.77 b	10.4 b	9.8 b
CMRR	47.4 dB	—	—	—	55 dB	50 dB
Shielding	No	Necessary	No	No	No	No

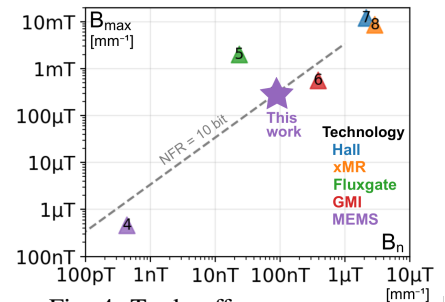


Fig. 4: Trade-off curve.